

# HST observations of star clusters in NGC 1023: Evidence for three cluster populations? <sup>1</sup>

Søren S. Larsen and Jean P. Brodie

*UC Observatories / Lick Observatory, University of California, Santa Cruz, CA 95064, USA*

[soeren@ucolick.org](mailto:soeren@ucolick.org) and [brodie@ucolick.org](mailto:brodie@ucolick.org)

## ABSTRACT

Using HST images we have carried out a study of cluster populations in the nearby S0 galaxy NGC 1023. In two WFPC2 pointings we have identified 221 cluster candidates. The small distance ( $\sim 9$  Mpc) combined with deep F555W and F814W images allows us to reach about two magnitudes below the expected turn-over of the globular cluster luminosity function. NGC 1023 appears to contain at least three identifiable cluster populations: the brighter clusters show a clearly bimodal color distribution with peaks at  $(V-I)_0 = 0.92$  and at  $(V-I)_0 = 1.15$  and in addition there are a number of fainter, more extended objects with predominantly red colors. Among the brighter clusters, we find that the blue clusters have somewhat larger sizes than the red ones with mean effective radii of  $R_e \sim 2$  and  $R_e \sim 1.7$  pc, respectively. These clusters have luminosity functions (LFs) and sizes consistent with what is observed for globular clusters in other galaxies. Fitting Gaussians to the LFs of the blue and red compact clusters we find turn-over magnitudes of  $M_{\text{TO}}(\text{blue}) = -7.58_{-7.36}^{+7.72}$  and  $M_{\text{TO}}(\text{red}) = -7.37_{-7.09}^{+7.50}$  in  $V$  and dispersions of  $\sigma_V(\text{blue}) = 1.12_{-1.03}^{+1.33}$  and  $\sigma_V(\text{red}) = 0.97_{-0.89}^{+1.25}$ . The fainter, more extended clusters have effective radii up to  $R_e \sim 10 - 15$  pc and their LF appears to rise at least down to  $M_V \sim -6$ , few of them being brighter than  $M_V = -7$ . We suggest that these fainter objects may have a formation history distinct from that of the brighter GCs.

*Subject headings:* galaxies: elliptical and lenticular, cD — galaxies: star clusters — galaxies: individual (NGC 1023)

## 1. Introduction

During the last two decades a large amount of information about globular cluster systems (GCSs) in other galaxies has been collected. One of the most remarkable findings is the apparent

---

<sup>1</sup>Based on observations with the NASA/ESA Hubble Space Telescope, obtained at the Space Telescope Science Institute, which is operated by the Association of Universities for Research in Astronomy, Inc. under NASA contract No. NAS5-26555.

constancy of the globular cluster luminosity function (GCLF), which is nearly always well fitted by a Gaussian-like function with a turn-over magnitude ( $M_{\text{TO}}$ ) at  $M_V \sim -7.5$  plus/minus a few tenths of a magnitude at most (Harris 1999) and a dispersion of  $\sigma_V \sim 1.2$ . Thus, the GCLF has gained much potential as a distance indicator. Note that the GCLF is Gaussian in *magnitude* units. When plotted in luminosity units it is well represented as a composite of two power-laws with a change in slope at a luminosity roughly corresponding to the turn-over magnitude (Harris and Pudritz 1994).

Another intriguing discovery is that many GCSs have bimodal color distributions, generally thought to represent GC populations of different metallicities and/or ages. Recent studies (Gebhardt and Kissler-Patig 1999; Kundu 1999) have shown this to be a very common phenomenon, providing evidence that many galaxies must have had several distinct episodes of star formation. The GCSs of a few galaxies such as M87 and NGC 1399 have even been suggested to contain three metallicity peaks (Lee and Geisler 1993). A number of scenarios have been suggested to account for the presence of several cluster populations in galaxies. These include formation of the metal-rich population by gas-rich mergers (Ashman and Zepf 1992), in late stages of a multi-phase collapse (Forbes, Brodie and Grillmair 1997), or accretion of the *metal-poor* population in giant ellipticals from less luminous galaxies (Côté, Marzke and West 1998; Hilker, Infante and Richtler 1999). However, no single theory can be said to satisfactorily account for all observed properties of globular cluster systems in different galaxies and the final answer may possibly lie in a combination of the above and/or other scenarios. A thorough discussion of various formation scenarios is given in van den Bergh (2000).

In spite of the advances and the vast amount of data collected, many fundamental questions about the properties of GCSs still remain to be answered. One of the most elusive problems has been to explain the constancy of the GCLF turn-over and it is still debated whether the LF of old GCSs can be explained by dynamical evolution from the power-law luminosity distribution that is observed in *young* cluster systems in mergers and starburst galaxies (Elmegreen and Efremov 1997; Whitmore et al. 1999; Zhang and Fall 1999; Fritze-v. Alvensleben 1999). In this respect it is important to study the faint wing of the GCLF ( $M_V > -7.5$ ) where the effects of dynamical evolution would be most pronounced. For most galaxies this remains a difficult task even with HST photometry, so although the turn-over magnitude may indeed be universal, much less is known about whether or not the shape of the GCLF is really constant, especially to fainter magnitudes.

In this paper we report the results of a study of star clusters in the nearby SB0 galaxy NGC 1023. The generic term “star clusters” is here preferred to “globular clusters” for reasons that will become apparent later. We adopt a distance modulus of  $m - M = 29.97 \pm 0.14$ , measured using planetary nebulae (Ciardullo, Jacoby and Harris 1991) and consistent with the HST Cepheid distance of another member of the same group, NGC 925 ( $m - M = 29.84 \pm 0.16$ , Silbermann et al. 1996). The GCLF turn-over is thus expected to be at  $V \sim 22.5$ , bright enough that we can reach at least two magnitudes below it with our HST data and probe the faint end of the GCLF. At the distance of NGC 1023,  $1''$  corresponds to 48 pc, so objects with sizes of a few pc (typical for globular clusters in the Milky Way and other galaxies) will appear relatively well resolved and

good estimates of their sizes can be obtained. For the interstellar absorption towards NGC 1023 we adopt  $E(B-V) = 0.061$  (Schlegel et al. 1998), corresponding to  $E(V-I) = 0.10$  and  $A_V = 0.19$  (Cardelli, Clayton and Mathis 1989). This is very similar to the  $E(B-V) = 0.06$  found by Kinman et al. (1982), as well as to the  $A_B$  value of 0.27 (equivalent to  $E(B-V) = 0.066$ ) given in the RC3 catalogue.

NGC 1023 is included in Arp’s *Atlas of Peculiar Galaxies* (Arp 1966) because of a small eastern companion, NGC 1023A. On optical images NGC 1023A looks like an extension of the main galaxy to the E, but its  $U-B$  color is noticeably bluer than that of NGC 1023 itself and implies that active star formation has proceeded in the companion until  $\sim 200$  Myr ago (Capaccioli et al. 1986). NGC 1023 is known to be rich in HI gas, possibly associated with the companion, and HI maps (Sancisi et al. 1984) show that the highest concentration of HI gas in the NGC 1023 system is indeed coincident with the location of NGC 1023A. The radial velocity of the HI gas near NGC 1023A is also consistent with the gas being associated with NGC 1023A (Capaccioli et al. 1986). Much of the remaining gas forms a ring-like structure around NGC 1023. Several other dwarf galaxies are known near NGC 1023 (Davies and Kinman 1984) and it seems plausible that the ongoing accretion of NGC 1023A may just be the most recent of several similar events that have taken place in the past. Such interactions could have had significant impacts on the star- and cluster formation history of NGC 1023 itself.

## 2. Data

WFPC2 images in the F555W and F814W filters were obtained in Cycle 6 for two pointings in NGC 1023, one with the Planetary Camera (PC) centered on the galaxy nucleus and another further to the East (Fig. 1). For both pointings the total integration time in each filter was 2400 sec, split into two integrations.

The two exposures for each pointing in each of the F555W and F814W filters were combined using the IRAF `imcombine` task with the `reject` option set to `crreject`, eliminating Cosmic Ray events. Prior to photometric analysis, we removed large-scale background variations by a two-step process: First, the images were smoothed with a  $15 \times 15$  box median filter and the smoothed images were then subtracted from the original set. Objects were detected on this first preliminary set of background-subtracted images using the `daofind` task in the DAOPHOT package (Stetson 1987) and the detected objects were subtracted from the original images using the `ishape` algorithm (Larsen 1999). `ishape` is capable of dealing with extended objects of varying sizes, in contrast to e.g. the `substar` task in DAOPHOT. The object-subtracted images were smoothed as before, resulting in a set of images with all small-scale variations removed, which were then subtracted from the original images to produce our final set of background-subtracted images for further analysis.

Input object lists for photometry were produced by running `daofind` on the background-subtracted images in both of the F555W and F814W bands and matching the two lists. As an

additional selection criterion, the background noise was measured directly on the image in an annulus around each object and only objects with a  $S/N > 3$  in both F555W and F814W within an aperture radius of 2 pixels were accepted. In this way we accounted for the varying background noise within the image.

Photometry was then obtained using the `phot` task in DAOPHOT. Because the *difference* between aperture corrections in different filters is quite independent of object size (Holtzman et al. 1996; Larsen 1999, see also Sect. 2.1), we used a small aperture radius ( $r = 2$  pixels) for  $V - I$  colors. Selection of the aperture for  $V$  magnitudes represented a more difficult compromise between eliminating systematic and random errors, but we found an  $r = 3$  pixels aperture to be a reasonable choice. The calibration to  $V$  and  $I$  band magnitudes was done following the procedure described in Holtzman et al. (1995).

A second run of `ishape` was also performed in order to get intrinsic sizes for all objects detected in the second pass. The HST PSF was modeled using the `TinyTim` simulator (Krist and Hook 1997) and King profiles with concentration parameter  $c = 30$  were assumed for the cluster profile models. Here  $c$  is the ratio between tidal and core radius. `ishape` produced estimates of the FWHM of each cluster, which were then converted to half-light radii. The `ishape` modeling also included convolution with the WFPC2 diffusion kernel.

In order to test the reliability of the cluster sizes we added artificial objects, generated by convolving the `TinyTim` PSF with King profiles of various FWHM values, to the NGC 1023 images. The sizes of the artificial objects were then remeasured using `ishape`. Repeating this experiment for artificial objects of different magnitudes, we found that the input cluster sizes could be reproduced with an accuracy of about  $\pm 30\%$  down to  $V = 24$ .

As a further check of `ishape` we compared our FWHM values with the  $\Delta_{0.5-3}$  index, originally defined by Schweizer et al. (1996) and since then used by many authors to measure sizes of extended objects on HST images. Fig. 2 shows the  $\Delta_{0.5-3}$  values versus FWHM estimates by `ishape` for objects with  $V < 24$ . A quite good, although not linear correlation exists, giving confidence to the cluster sizes measured by `ishape`. We also checked the `ishape` cluster sizes from F555W and F814W images against each other, again providing excellent agreement.

Because of possible systematic differences between aperture corrections and object sizes measured on the PC and WF camera chips, and because of the very high surface brightness in the central parts of NGC 1023, we only considered objects in the WF chips. Inspection by eye revealed at most  $\sim 10$  cluster candidates on the PC chip of the central pointing down to the detection limit.

## 2.1. Aperture corrections

In order to measure  $\Delta m_{2 \rightarrow 5}$  and  $\Delta m_{3 \rightarrow 5}$  aperture corrections for extended sources from the  $r = 2$  and  $r = 3$  pixels apertures to the Holtzman et al. (1995)  $r = 5$  pixels reference aperture, we

convolved the `TinyTim` PSF with King  $c = 30$  and MOFFAT15 (Larsen 1999) profiles of different FWHM values. The aperture corrections were then obtained by carrying out aperture photometry on the convolved model profiles, measuring the differences in the fluxes through various apertures. The experiment was carried out for a number of different FWHM values for the model profiles, ranging between 0.1 and 2.0 pixels (0.5 – 10 pc at the assumed distance of NGC 1023). The FWHM can be converted to effective radii ( $R_e$ ) by multiplying with 1.48 for the King  $c = 30$  profiles and by 1.13 for the MOFFAT15 profiles.

The aperture corrections measured in this way are listed in Table 1 for the F555W band and for the difference F555W–F814W. In addition to the  $\Delta m_{2 \rightarrow 5}$  and  $\Delta m_{3 \rightarrow 5}$  corrections between the  $r = 5$  reference aperture and the apertures used for our photometry, Table 1 also lists aperture corrections from  $r = 5$  to  $r = 30$  pixels.

Not surprisingly, the aperture corrections in F555W depend strongly on object size. For point sources the  $\Delta m_{3 \rightarrow 5}(\text{F555W})$  correction is  $-0.060$  mag, increasing to  $-0.15$  for a King  $c = 30$  profile with FWHM=0.50 pixels and reaching  $-0.43$  mag for FWHM=2.0 pixels. For a given FWHM, the aperture corrections for the MOFFAT15 profiles are somewhat smaller than for the King  $c = 30$  profiles because a larger fraction of the flux is contained in the wings of the King  $c = 30$  profile. For a King profile with a smaller concentration parameter, the aperture corrections would be smaller for any given FWHM.

A correction of  $-0.1$  mag from the  $r = 5$  pixels aperture to infinity is implicit in the standard calibration procedure, in good agreement with our results for point sources listed in Table 1. According to Holtzman et al. (1995), this correction is nearly independent of the choice of filter, small changes in telescope focus etc. However, for extended objects a larger fraction of the light falls outside the  $r = 5$  aperture, amounting to an error of about  $-0.4$  mag for a FWHM of 2 pixels ( $R_e = 14$  pc) if no correction is applied.

Although the aperture corrections in one filter depend strongly on object size, *colors* can be measured with much better precision. For point sources we find an aperture correction  $\Delta m_{2 \rightarrow 5}(\text{F555W} - \text{F814W})$  of 0.031 mag for the  $V - I$  colors, in good agreement with other authors (Puzia et al. 1999; Whitmore et al. 1997). The correction depends only weakly on the object size, implying that systematic errors in  $V - I$  color are small ( $\lesssim 0.01$  mag) even for objects with effective radii up to  $\sim 15$  pc. This remains true also when the correction from  $r = 5$  to infinity is considered, which is constant within the uncertainties. The  $V - I$  aperture corrections from  $r = 5$  to  $r = 30$  given in Table 1 are, strictly speaking, only valid for the idealized case where the background level can be determined with high precision. In practice, small uncertainties in the background determination and in the object profiles will generally overshadow the small changes in the  $V - I$  aperture corrections from  $r = 5$  to infinity as a function of object size.

Considering that Milky Way globular clusters typically have  $R_e \sim 3$  pc (Harris 1996), we adopted an  $\Delta m_{3 \rightarrow 5}(\text{F555W})$  aperture correction of  $-0.14$  mag. This aperture correction is probably accurate to about 0.1 mag for objects with intrinsic  $R_e \lesssim 5$  pc, but larger objects will be

systematically too faint by up to several tenths of a magnitude. The total  $V$  error for an  $R_e = 14$  pc object will amount to about 0.7 mag. For  $V - I$  we use a correction of 0.026, which should lead to systematic errors of no more than about 0.01 mag or so.

## 2.2. Completeness

Because of the relatively small distance, clusters in NGC 1023 appear quite well resolved on our HST images. This requires that special attention be paid to completeness corrections and their dependence on the angular extent of the objects. We carried out completeness tests by adding synthetically generated objects to the science frames and checking how many of the artificial objects were recovered by a subsequent photometry run as a function of magnitude. The tests were repeated for a number of different object sizes, using the `TinyTim` PSF convolved with King profiles of FWHM ranging between 0.25 and 2 pixels, corresponding to  $R_e = 1.8 - 14.2$  pc.

The results of the completeness tests are shown in Fig. 3. The 50% completeness limit for *point sources* (i.e., the pure `TinyTim` PSF) is at  $V \approx 26.2$ , but for more extended objects the curves shift rapidly to the left in the diagram, indicating that the 50% limit for objects with  $R_e = 14$  pc is at  $V \approx 24.5$ , about two magnitudes brighter than for point sources.

The curves in Fig. 3 represent the *average* completeness functions for each field. However, the completeness also depends on the background level. Because the background level increases strongly towards the center of NGC 1023, a radial dependence may be expected for the completeness functions. In order to test this, we performed another set of completeness tests by adding artificial objects to a number of purely synthetic images with different background levels, including photon shot noise as well as a contribution from “read-out noise” in the synthetic images. This allowed us to check how the completeness functions depend on the background level and, by comparison with the surface brightness profile of NGC 1023, on the distance from the center of the galaxy. Fig. 4 shows the 50% completeness limit obtained from these tests as a function of distance  $D$  from the center of NGC 1023 along the major axis, for objects with  $R_e = 2$  pc, 7 pc and 14 pc. From these tests we expect the 50% completeness limit to be below  $V = 24$  for objects with  $R_e < 14$  pc at  $D \gtrsim 20''$ .

Note that the  $x$ -axes in Figs. 3 and 4 refer to the synthetic *input* magnitudes which, for extended objects, will be somewhat brighter than the magnitudes actually measured in our  $r = 3$  pixels aperture. Therefore, since extended objects are actually brighter than they appear, the detection of extended objects with a given *apparent* magnitude will be more efficient than what appears from the curves in Figs. 3 and 4.

### 3. Results

Fig. 5 shows a  $(V-I)_0, V$  color-magnitude diagram for all objects detected in the two WFPC2 pointings down to  $V = 25$ , corrected for Galactic foreground extinction. Below  $V = 25$  the photometric errors become very large, exceeding 0.20 in  $V-I$  so we do not consider objects fainter than this limit. For further analysis we selected globular cluster (GC) candidates as objects in the color interval  $0.75 < (V-I)_0 < 1.40$  (dashed lines) and  $20 < V < 25$ , resulting in a total of 221 GC candidates.

#### 3.1. Colors and sizes: three cluster populations?

Already a casual inspection of the color-magnitude diagram in Fig. 5 reveals a clearly bimodal color distribution. A homoscedastic KMM test (Ashman, Bird and Zepf 1994) confirms bimodality at the  $> 99.9\%$  confidence level with peaks at  $(V-I)_0 = 0.93$  and  $(V-I)_0 = 1.19$  for the sample of GC candidates, corresponding to metallicities of  $[\text{Fe}/\text{H}] = -1.5$  and  $[\text{Fe}/\text{H}] = -0.6$  (Kissler-Patig et al. 1998). The KMM test assigns 45.7% of the objects to the blue peak and 54.3% to the red one. As a formal dividing line between “blue” and “red” clusters we adopt  $(V-I)_0 = 1.05$ .

Fig. 6 shows the sizes as a function of  $(V-I)_0$  color for cluster candidates brighter than  $V = 24$  (145 objects). Histograms of the  $R_e$  distributions for red ( $(V-I)_0 < 1.05$ ) and blue clusters ( $(V-I)_0 > 1.05$ ) are in Fig. 7. The size distribution of blue GC candidates peaks at  $R_e \sim 2$  pc, while the scatter in the size distribution for the red GC candidates is much larger with a peak at  $R_e \sim 1$  pc and a tail extending up to  $R_e \sim 15$  pc. For the most compact sources, the effective radii are not very sensitive to the specific choice of model profile (Larsen 1999). However, for the more extended sources the derived  $R_e$  values depend on the adopted model profiles. If we use MOFFAT15 instead of King  $c = 30$  models the sizes of clusters larger than  $R_e \sim 5$  pc are reduced by roughly 25%, while the  $R_e$  values for the compact GCs remain essentially unaffected. The numbers given throughout this paper are based on King  $c = 30$  models.

Fig. 6 suggests a division of the clusters into two groups based on their sizes, splitting at  $R_e = 7$  pc or so. In the following, we thus distinguish between “compact” and “extended” objects as objects with  $R_e < 7$  pc and  $R_e \geq 7$  pc, respectively. This results in 116 and 29 objects being assigned to the compact and extended groups. The exact size cut is of little importance; if we had used 5 pc instead of 7 pc then the number of compact and extended objects would have been 111 and 34. Leaving out the extended objects and re-running the KMM test, the color distribution is still bimodal at the  $> 99.9\%$  confidence level and the two peaks are now at  $(V-I)_0 = 0.92$  and  $(V-I)_0 = 1.15$ . Just taking the average colors of the blue and red clusters gives  $(V-I)_0 = 0.92$  and  $(V-I)_0 = 1.17$ , in excellent agreement with the KMM estimates. The relative numbers of blue and red objects are now 57.5% and 42.5%, confirming that a larger fraction of the red objects have  $R_e > 7$  pc.

The average sizes of blue and red compact clusters are 2.0 pc and 1.7 pc, while the median sizes are 1.8 and 1.1 pc, respectively. Even for objects in the “compact” category, there is a significant tail up to  $R_e \sim 5$  pc for both blue and red clusters. This is no different from our own Galaxy (van den Bergh 1996) and similar size distributions have also been noted in a number of other galaxies (Kundu 1999).

Fig. 8 shows a color-magnitude diagram for the same objects as in Fig. 5, but now with symbol sizes proportional to the object sizes derived by `ishape`. For a few objects (mostly faint ones with  $V > 24$ ) the `ishape` fits failed to converge and hence such objects do not appear in Fig. 8. Very compact objects with  $R_e \lesssim 0.2$  pc (presumably foreground stars) scatter all over the diagram and are not very numerous. The extended red objects are *clearly fainter* than the compact red objects, most of them having  $V > 23$ , and appear to constitute a separate population, distinct from the normal globular clusters in NGC 1023.

The fact that clusters larger than about 7 pc are predominantly red and faint is also demonstrated by Fig. 9 which shows the cluster  $V$  magnitudes as a function of their sizes. Red clusters are shown with plus markers and blue clusters with triangles. The plot contains a few large blue objects fainter than  $V = 24$ , but the size estimates become increasingly uncertain below  $V = 24$  and some of these objects may well be contaminating background galaxies. Fig. 9 is qualitatively quite similar to the corresponding plots for globular clusters in the Milky Way (Fig. 1 in van den Bergh (1996)). Note, however, that the large clusters in our own galaxy are predominantly *metal-poor* while the opposite seems to be the case in NGC 1023 (assuming that a red color indicates high metallicity). Also, the large clusters are much more numerous in NGC 1023.

### 3.2. Comparison field

To check the contamination by foreground and background objects we obtained photometry for a comparison field located about 2 degrees from NGC 1023, using HST archive data (proposal ID 6254, PI: E. Groth). The comparison data consist of  $2 \times 1300$  s integrations in each of the F606W and F814W filters and should thus be roughly as deep as our NGC 1023 data, except for the wider bandpass of the F606W filter and the lower background far from NGC 1023. Both effects will tend to make the comparison data more complete at faint magnitudes than our NGC 1023 data.

The  $V - I$  color-magnitude diagram for the comparison field is shown in Fig. 10. Without applying any size cut, the comparison field contains 16 objects in the color-magnitude range that confines our GC candidates, i.e.  $0.75 < V - I < 1.40$  and  $20 < V < 25$ . Since our NGC 1023 dataset consists of two pointings, we may thus expect about 32 contaminating objects out of the total number of 221 GC candidates. However, most of the contaminating objects are quite faint and for  $V < 24$  we find only 5 objects in the comparison field in the GC candidate color range. Of these, 3 fall into the blue category and 2 in the red. Contamination is thus expected to be a minor

problem above  $V \sim 24$ . Comparison of Figs. 5 and 10 also shows that objects outside the GC color range can be easily explained as foreground and/or background sources.

### 3.3. Spatial distributions

The spatial distributions of different object types are illustrated in Fig. 11, which shows contours of an optical image of NGC 1023 (from the Digital Sky Survey) overlaid with our WFPC2 pointings. The two upper panels show the distribution of red (left) and blue (right) compact objects. The lower left panel shows the faint extended objects with  $R_e > 7$  pc, and the lower right panel contains all objects in the three other panels added together. Since size information is used in producing these plots, all objects are brighter than  $V = 24$ .

The spatial distributions of compact and extended objects clearly differ. The extended sources are not nearly as concentrated towards the center of the galaxy and appear to be associated with the *disk* of NGC 1023. The high degree of alignment with the isophotes of NGC 1023 makes it unlikely that they are background sources like, for example, a distant galaxy cluster. Even for the extended objects, our data are expected to be more than 50% complete for  $V < 24$  (Sect. 2.2) except at distances smaller than about  $20''$  from the nucleus of NGC 1023 along the major axis. This corresponds roughly to the edge of the PC chip (the small boxes in Fig. 11) and it is therefore clear that completeness effects cannot explain the observed differences in the radial distributions of various object types.

Among the compact GCs, we note that the distribution of red clusters seems to be more flattened than that of blue ones. A similar result was found for NGC 3115 by Kundu and Whitmore (1998) who suggested that the red (metal-rich) GCs are associated with a thick-disk like population, while the blue (metal-poor) clusters are halo objects.

### 3.4. Luminosity distributions

The luminosity functions for the different object types are shown in Fig. 12. The overall appearance of the luminosity distributions for compact objects appears to be consistent with a maximum at  $V \sim 22.3$ , roughly as expected for a “standard” Gaussian GCLF. Fig. 13 shows the luminosity functions of red and blue objects in the comparison field. We remind the reader that the luminosity functions in Fig. 13 should be multiplied by a factor of 2 (only one comparison field but two science fields) before comparison with Fig. 12. For both the red and blue objects, significant contamination clearly sets in below  $V = 24$  and many of the excess faint red objects in NGC 1023 (relative to the standard GCLF) below this magnitude are likely contaminants.

We carried out maximum-likelihood fits of Gaussian and Student’s  $t_5$  functions (Secker 1992) to the luminosity functions of objects with  $V < 24$ . Incompleteness effects are expected to be

negligible (especially for compact objects) above this magnitude limit, which is  $\sim 1.5$  mag below the expected turn-over and we should thus be able to obtain quite robust estimates of the parameters ( $M_{\text{TO}}(V)$  and  $\sigma_V$ ) of the GCLFs. The results are listed in Table 2 for red and blue compact clusters separately, for the combined sample of red and blue clusters, and for all cluster candidates including the extended red objects. A Gaussian fit yields  $M_{\text{TO}}(V) = -7.37_{-7.09}^{+7.50}$  and  $M_{\text{TO}}(V) = -7.58_{-7.36}^{+7.72}$  for the red and blue clusters, respectively, while the dispersions are  $\sigma_V = 0.97_{0.89}^{1.25}$  and  $1.12_{1.03}^{1.33}$ . If red and blue clusters are fitted simultaneously we get  $M_{\text{TO}}(V) = -7.48_{-7.32}^{+7.59}$  and  $\sigma_V = 1.07_{1.00}^{1.24}$ . Fitting a  $t_5$  function we get nearly the same turn-over magnitudes and, as expected (Secker 1992), somewhat narrower dispersions.

Within the error bars, the turn-over magnitudes and dispersions of the red and blue GCs are thus compatible with a standard GCLF, although the red GCs formally appear to have a somewhat narrower dispersion and a slightly fainter turn-over magnitude. The fact that the red GCs tend to have fainter turn-over magnitudes than blue ones has also been noted in other galaxies like e.g. NGC 3115 (Kundu and Whitmore 1998). We also used a Kolmogorov-Smirnov test (Lindgren 1962) to test how well the data are actually fitted by the Gaussian and  $t_5$  functions, as indicated by the  $P$  values in Table 2.  $P$  gives the probability that the data are drawn from parent distributions with the specified parameters. The blue compact clusters are very well fitted by both the Gaussian ( $P = 0.991$ ) and the  $t_5$  function ( $P = 0.999$ ), with the  $t_5$  function being slightly preferred over the Gaussian as was also found by Secker (1992) for Milky Way and M31 globular clusters. For the red clusters, on the other hand, both the Gaussian and the  $t_5$  function provide a quite poor fit to the data with  $P$  values of 0.352 and 0.529 although the  $t_5$  function is again preferred.

We also compared the luminosity functions of the red and blue compact populations directly using a two-population Kolmogorov-Smirnov test. Such a test is independent of any assumptions about the LF. Again leaving out clusters with  $V > 24$  in order to obtain as pure a sample of “true” globular clusters as possible, the  $D_n$  statistics of the test is 0.154. This corresponds to a 51% probability that the two cluster populations have the same luminosity function. The test is thus inconclusive as to whether or not the two compact cluster populations have the same luminosity function. This remains true even if the K-S test is performed only on a brighter subsample of the clusters.

The *extended* red objects do have a quite different luminosity function from a standard Gaussian (lower left panel), increasing at least down to  $V \sim 24$ . Because of extendedness of these objects, incompleteness effects have already set in at  $V \sim 24.5$  or so (cf. Figs. 3 and 4), so it remains uncertain how their luminosity function behaves at fainter magnitudes. With typical effective radii of the order of 10–15 pc (Fig. 6), the  $V$  magnitudes of the extended objects are probably underestimated by  $\sim 0.5$  mag (Table 1) although the colors remain unaffected by object size. In any case, the differences in the luminosity and color distributions of extended and compact objects clearly cannot be accounted for by instrumental effects.

The lower right panel of Fig. 12 displays the combined luminosity function of all cluster can-

didates. Even without performing any statistical tests it is clear that a Gaussian or a  $t_5$  function provide a poor fit to the combined LF, mostly due to the presence of the extended red objects. Indeed, the maximum-likelihood fit returns a turn-over magnitude of  $M_{\text{TO}}(V) = -6.98_{-6.85}^{+7.13}$  for the Gaussian and  $M_{\text{TO}}(V) = -7.07_{-6.95}^{+7.21}$  for the  $t_5$  function, half a magnitude fainter than for the compact clusters alone.

Bearing in mind that the magnitudes for extended objects measured in the  $r = 3$  pixels aperture are probably too faint by  $\sim 0.5$  mag (Sect. 2.1), the true luminosity function of all objects may look somewhat different from the lower right panel of Fig. 12. We added a rough correction of  $-0.5$  mag to the  $V$  band magnitudes of the extended objects in order to check how this would affect the combined luminosity function. However, applying the same magnitude limit of  $V = 24$  to the corrected sample would then lead to a larger number of faint objects with uncertain sizes and photometry, possibly resulting in unreliable LF fits. We therefore restricted the LF fits of the corrected sample to objects brighter than  $V = 23.5$ . For a Gaussian fit we then obtained a turn-over at  $M_{\text{TO}}(V) = -7.19_{-6.77}^{+7.35}$ , which is somewhat closer to the value expected for a “standard” Gaussian GCLF. If we apply the same  $V = 23.5$  magnitude cut to the original *non-corrected* photometry, we obtain  $M_{\text{TO}}(V) = -7.25_{-6.85}^{+7.42}$  for a Gaussian fit. As demonstrated by these experiments, the LF fits to the full cluster sample including extended objects are quite unstable and depend strongly on the magnitude cuts and various corrections. This is not too surprising, considering that we are attempting to fit a Gaussian function to a non-gaussian distribution.

Until it is better understood how common such extended faint clusters are and what fraction of the total GC population they constitute in different galaxies, they could pose a potential problem for the use of GCLFs as “standard candles”. However, Gaussian or  $t_5$  fits to GCLFs should still be relatively secure if constrained to objects brighter than about 1 mag below the turn-over.

#### 4. Discussion

In summary, NGC 1023 appears to contain at least three identifiable cluster populations: 1) blue globular clusters with a standard Gaussian luminosity function and with an average  $R_e \sim 2$  pc. The mean color is  $\langle V-I \rangle_0 = 0.92$ . 2) red globular clusters ( $\langle V-I \rangle_0 = 1.15$ ) with smaller sizes ( $R_e \sim 1.7$  pc), whose LF may have a somewhat fainter turn-over magnitude and a slightly narrower dispersion. 3) A population of faint extended sources with  $R_e \sim 10 - 15$  pc ( $R_e \sim 7 - 10$  pc when using MOFFAT15 model profiles), which are predominantly red.

##### 4.1. The classical globular clusters

Concerning sizes and color distributions of the normal compact clusters, the GCS of NGC 1023 appears to be quite similar to what has been observed in a number of other early-type galaxies such as NGC 4472, M87 and NGC 3115 (Kundu and Whitmore 1998; Kundu et al. 1999; Puzia

et al. 1999). Deviation from unimodality in the NGC 1023 cluster colors was already hinted at by Gebhardt and Kissler-Patig (1999) and is now very clearly confirmed by our deeper data. The fact that red GCs tend to have smaller effective radii than their blue counterparts has also been observed in the above mentioned galaxies, but the small distance of NGC 1023 and our deep HST data add further confidence to this result.

The overall characteristics of the cluster systems in a number of early-type galaxies thus appear to be quite similar, providing support to the idea that the same mechanisms governed formation of the globular cluster systems in a wide variety of galaxies. In particular, any scenario that attempts to explain the presence of bimodal color distributions must account for the presence of this phenomenon in cDs as well as lenticulars and other galaxy types.

Ultimately, one also needs to understand the size difference between metal-poor and metal-rich clusters – perhaps this is evidence for different physical conditions in the parent clouds, or maybe it indicates that the different cluster populations have been subject to different destruction processes, e.g. because of different kinematics. Obviously, a better understanding of the physics of cluster formation and evolution is needed in order to address the first possibility, while insight into the kinematics of cluster sub-populations may be gained by spectroscopy of large cluster samples. It is worth pointing out, though, that all theoretical studies so far indicate that the half-light radius for any individual cluster is a very stable quantity and does not change much over the lifetime of the cluster (Spitzer 1987; Meylan and Heggie 1997). If the size distributions of red and blue clusters in NGC 1023 (and other galaxies) originated from the same parent distribution, quite substantial differences in the destruction mechanisms and/or dynamical evolution of the two subpopulations would have been necessary to make their present-day size distributions differ as much as is observed. At the same time, these mechanisms would have to act in such a way that the blue and red GCs would still retain roughly similar luminosity functions, although Vesperini (2000) has recently argued that the GCLF is relatively stable against dynamical evolution.

Alternatively, different cluster sizes would be the result of different physical conditions at the time of cluster formation. Our understanding of cluster formation is currently in a rather rudimentary state, but in the case of the Milky Way, McLaughlin (1999) has suggested that the observed correlation between sizes of globular clusters and galactocentric distance could be explained by the progenitor clouds closer to the center having higher binding energies. How this relates to the size differences between red and blue GC populations in NGC 1023 and other early-type galaxies is not entirely clear though, especially since no correlation between galactocentric distance and cluster sizes appears to exist in galaxies like NGC 4472 (Puzia et al. 1999). One could speculate that, since the red (metal-rich) population is likely to have formed somewhat later than the blue one, the key issue may here be a *temporal* rather than *spatial* change in the cluster forming environment.

## 4.2. A third cluster population?

A major peculiarity about the NGC 1023 cluster system is the presence of a number of fainter objects with much larger average effective radii than the “genuine” globular clusters. Most of these objects are quite red with colors comparable to the red GC population,  $(V-I)_0 \sim 1.2$ . Because the comparison field does not contain similar objects, and because of the alignment of their spatial distribution with the isophotes of NGC 1023 itself, we feel confident that these objects are indeed star clusters in NGC 1023. A chance alignment with e.g. a distant galaxy cluster appears to be highly unlikely, not only because of the low probability of such an alignment by itself, but even more so because the background cluster would have to have an annular shape.

The red colors of these objects are probably real and not due to e.g. reddening by interstellar absorption. First, reddening is not expected to be much of an issue in a galaxy of this type. This is confirmed by the absence of any significant FIR emission – the  $12\mu$  flux as measured by the IRAS satellite is only 0.16 Jy (Rice et al. 1988) and in the remaining IRAS bands only upper limits exist, so the presence of any significant amount of dust is ruled out. Furthermore, although the NGC 1023 system does possess significant amounts of HI gas, most of it is located far outside the main body of NGC 1023. Finally, interstellar absorption could not account for the *extendedness* of the faint clusters.

What is the nature of the faint extended clusters? Generally, they are too bright to be normal open clusters. For ages  $> 1$  Gyr, the Lyngå (1987) catalog lists no open clusters in the Milky Way brighter than  $M_V \sim -4$ . Furthermore, open clusters are not particularly large, with mean and median radii of 2.7 pc and 1.9 pc, respectively (Lyngå 1982). Hodge (1979) finds larger sizes for open clusters in M31, but notes that his sample is biased towards large clusters because of resolution limits. Hence, the extended clusters in NGC 1023 are too bright and too extended to be normal open clusters.

The  $V$  range spanned by the extended objects (23 – 24) corresponds to absolute magnitudes between  $-6$  and  $-7$ , well within the range spanned by *globular* clusters in our own and other galaxies and nearly reaching the peak of the standard GCLF. Our magnitudes for the extended objects are actually likely to be too *faint* by up to several tenths of a magnitude because of a larger fraction of light falling outside the  $r = 3$  aperture (Sect. 2.1). The closest counterparts in the Milky Way would be the Palomar-type globular clusters found in the outer part of the Galactic halo. Actually, most globular clusters in the Milky Way with *core* radii  $R_c > 3$  pc are known to be systematically fainter than globular clusters with  $R_c < 3$  pc, very few of them being brighter than  $M_V = -7$  (van den Bergh 1983, 1996). However, the extended clusters in NGC 1023 appear to be relatively *metal-rich* whereas the extended clusters in the outer halo of the Milky Way are metal-poor.

Concerning the origin of the extended red clusters, we may speculate that they could be related to accretion of satellite galaxies. In particular, ground-based images reveal the presence of two bright blue condensations near the center of the companion NGC 1023A which, unfortunately,

were not included on our WFPC2 pointings. These blue objects were already noted by Davies and Kinman (1984) who suggested they might be supergiant stars, but they are clearly extended and ground-based photometry and spectroscopy suggest ages on the order of  $\sim 0.5$  Gyr (Larsen et al., in preparation). Therefore NGC 1023A must have had an active star formation history until quite recently and a number of clusters could conceivably have been stripped from the companion and ended up in the disk of NGC 1023 during the last few 100 Myr or so. If NGC 1023A used to be a cluster-rich LMC-like galaxy, this scenario may not be entirely unlikely. One problem with this scenario is the red colors of the extended clusters, indicating relatively high metallicities. This could, perhaps, be explained if the extended clusters were *formed* in the disk of NGC 1023 when sufficient gas was still available, possibly triggered by interaction processes, rather than simply being accreted.

It would be highly desirable to shed more light on these questions with observations of similar objects in other galaxies. However, to our knowledge no extended, faint red clusters like those in NGC 1023 have previously been identified in any other early-type galaxy. The main point, of course, is that these objects are relatively *faint* and thus difficult to detect, and that high angular resolution is needed to obtain any information on cluster sizes. Therefore, only deep HST observations of nearby ( $\lesssim 10$  Mpc) galaxies would reveal such objects and they would, so far, have escaped detection even in HST studies of Virgo cluster galaxies. Until now, only one other early-type galaxy close enough for detection of extended clusters similar to those in NGC 1023 has had sufficiently deep HST photometry, namely NGC 3115 (Kundu and Whitmore 1998). However, Kundu and Whitmore (1998) did not report any such objects in their study of this galaxy. In order to check if they might have been overlooked, we re-examined the archive data and found that extended faint objects are indeed absent in NGC 3115.

## 5. Summary and conclusions

We have obtained deep WFPC2 photometry for star clusters in the nearby lenticular galaxy NGC 1023, reaching two magnitudes below the expected turn-over of the globular cluster luminosity function. Our  $V-I$  photometry reveals a very clearly bimodal color distribution with peaks at  $(V-I)_0 = 0.92$  and  $(V-I)_0 = 1.15$ , respectively. We also identified a number of red objects with larger effective radii than the brighter GCs and a luminosity function that rises at least down to  $M_V \sim -6$  (assuming the objects are at the distance of NGC 1023). A comparison field located about 2 degrees from NGC 1023 shows no such objects. Moreover, the spatial distribution of faint extended objects is well aligned with the isophotes of NGC 1023, indicating a very high probability that they are star clusters in the disk of NGC 1023.

The blue GC population has a luminosity function that is consistent at the 99% confidence level with a “standard” Gaussian GCLF with  $M_{\text{TO}}(V) = -7.58_{-7.36}^{+7.72}$  and  $\sigma_V = 1.12_{-1.03}^{+1.33}$ . A  $t_5$  function provides an even better fit, with  $M_{\text{TO}}(V) = -7.56_{-7.37}^{+7.70}$  and  $\sigma_V = 0.99_{-0.90}^{+1.20}$  at the 99.9% confidence level. The average effective radius of the blue GCs is  $\sim 2$  pc, comparable to (but perhaps slightly

smaller than) that seen in the Milky Way and other galaxies. The LF of the red GC population may have a somewhat narrower dispersion and a peak magnitude about 0.2 mag fainter than for the blue GC population, but is not very well fitted by either a Gaussian or a  $t_5$  function. On the average, the brighter red GCs have  $R_e \sim 1.7$  pc, or about 15% smaller than for the blue GCs.

The spatial, color and luminosity distributions of *extended* clusters with  $R_e > 7$  pc are clearly different from those of compact “genuine” globulars. We suggest that the faint extended red clusters may have their origin in accretion processes with companion galaxies, similar to the ongoing interaction with the dwarf NGC 1023A. Because of the extended red clusters, the combined luminosity function of all cluster candidates in NGC 1023 deviates significantly from a standard Gaussian GCLF. If such objects are common in other galaxies, this could potentially lead to problems in using the GCLF as a standard candle.

This work was supported by HST grant GO.06554.01-95A, National Science Foundation grant number AST9900732 and Faculty Research funds from the University of California, Santa Cruz. We thank Duncan Forbes and John Huchra for useful comments and suggestions, Carl Grillmair and Ken Freeman for their support, and the anonymous referee for a detailed and constructive report which helped significantly improve the paper.

## REFERENCES

Arp, H. C. 1966, ApJS, 14, 1

Ashman, K. M., and Zepf, S. E. 1992, ApJ, 384, 50

Ashman, K. M., Bird, C. M., and Zepf, S. E. 1994, AJ, 108, 2348

Capaccioli, M., Lorenz, H., and Afanasjev, V. L. 1986, A&A, 169, 54

Cardelli, J. A., Clayton, G. C. and Mathis, J. S. 1989, ApJ, 345, 245

Ciardullo, R., Jacoby, G. H., and Harris, W.E. 1991, ApJ, 383, 487

Côté, P., Marzke, R. O., and West, M. J. 1998, ApJ, 501, 554

Davies, R. D., and Kinman, T. D. 1984, MNRAS, 207, 173

Elmegreen, B. G., and Efremov, Yu. N. 1997, ApJ, 480, 235

Forbes, D. A., Brodie, J. P., and Grillmair, C. J. 1997, AJ, 113, 1652

Fritze-v. Alvensleben, U. 1999, A&A, 342, L25

Gebhardt, K., and Kissler-Patig, M. 1999, AJ, 118, 1526

Harris, W. E., and Pudritz, R. E. 1994, *ApJ*, 429, 177

Harris, W. E. 1996, *AJ*, 112, 1487

Harris, W. E. 1999, in: “Globular Clusters”, Cambridge Contemporary Astrophysics, eds. C. M. Rogers, I. Pérez Fournón and F. Sánchez, Cambridge University Press

Hilker, M., Infante, L., and Richtler, T. 1999, *A&A Suppl.*, 138, 55

Hodge, P. W. 1979, *AJ*, 84, 744

Holtzman, J. A., Burrows, C. J., Casertano, S., et al. 1995, *PASP*, 107, 1065

Holtzman, J. A., Watson, A. M., Mould, J. R., et al. 1996, *AJ*, 112, 416

Kinman, T. D., Mahaffey, C. T., and Wirtanen, C. A. 1982, *AJ*, 87, 314

Kissler-Patig, M., Brodie, J. P., Schroder, L. et al., 1998, *AJ*, 115, 105

Krist, J., and Hook, R. 1997, “The Tiny Tim User’s Guide”, STScI

Kundu, A., and Whitmore, B. C. 1998, *AJ*, 116, 2841

Kundu, A. 1999, PhD thesis, Univ. of Maryland

Kundu, A., Whitmore, B. C., Sparks, W. B., et al., 1999, *AJ*, 513, 733

Larsen, S. S. 1999, *A&A Suppl.*, 139, 393

Lee, M. G., and Geisler, D. 1993, *AJ*, 106, 493

Lindgren, B. W. 1962, “Statistical Theory”, Macmillan Company, New York

Lyngå, G. 1982, *A&A*, 109, 213

Lyngå, G. 1987, “Catalogue of Open Cluster Data”, 5th edition, available via Centre de Données Stellaires, Strasbourg, <http://cdsweb.u-strasbg.fr>

McLaughlin, D., 1999, in: “Proceedings of the 33rd ESLAB Symposium, Star Formation from the Small to the Large Scale”, eds. F. Favata, A. A. Kaas, and A. Wilson, astro-ph/0002087

Meylan, G., and Heggie, D. C. 1997, *A&A Rev.*, 8, 1

Puzia, T. H., Kissler-Patig, M., Brodie, J. P., and Huchra, J. P. 1999, *AJ*, 118, 2734

Rice, W., Carol, J., Lonsdale, Soifer, B.T., et al. 1988, *ApJS*, 68, 91

Sancisi, R., van Woerden, H., Davies, R. D., and Hart, L. 1984, *MNRAS*, 210, 497

Schlegel, D. J., Finkbeiner, D. P., and Davis, M. 1998, *ApJ*, 500, 525

Schweizer, F., Miller, B. W., Whitmore, B. C., and Fall, S. M. 1996, AJ, 112, 1839

Secker, J. 1992, AJ, 104, 1472

Silbermann, N.A., Harding, P., Madore, B. F., et al. 1996, ApJ, 470, 1

Spitzer, L. 1987, “Dynamical Evolution of Globular Clusters”, Princeton Series in Astrophysics, Princeton University Press

Stetson, P. B. 1987, PASP, 99, 191

van den Bergh, S., 1983, PASP, 94, 640

van den Bergh, S., 1996, AJ, 112, 2634

van den Bergh, S., 2000, PASP, (in press), astro-ph/0006167

Vesperini, E., 2000, MNRAS, (in press), astro-ph/0007266

Whitmore, B. C., Miller, B. W., Schweizer, F., and Fall, S. M. 1997, AJ, 114, 1797

Whitmore, B. C., Zhang, Q., Leitherer, C., et al. 1999, AJ, 118, 1551

Zhang, Q. and Fall, S. M. 1999, ApJ, 527, L81

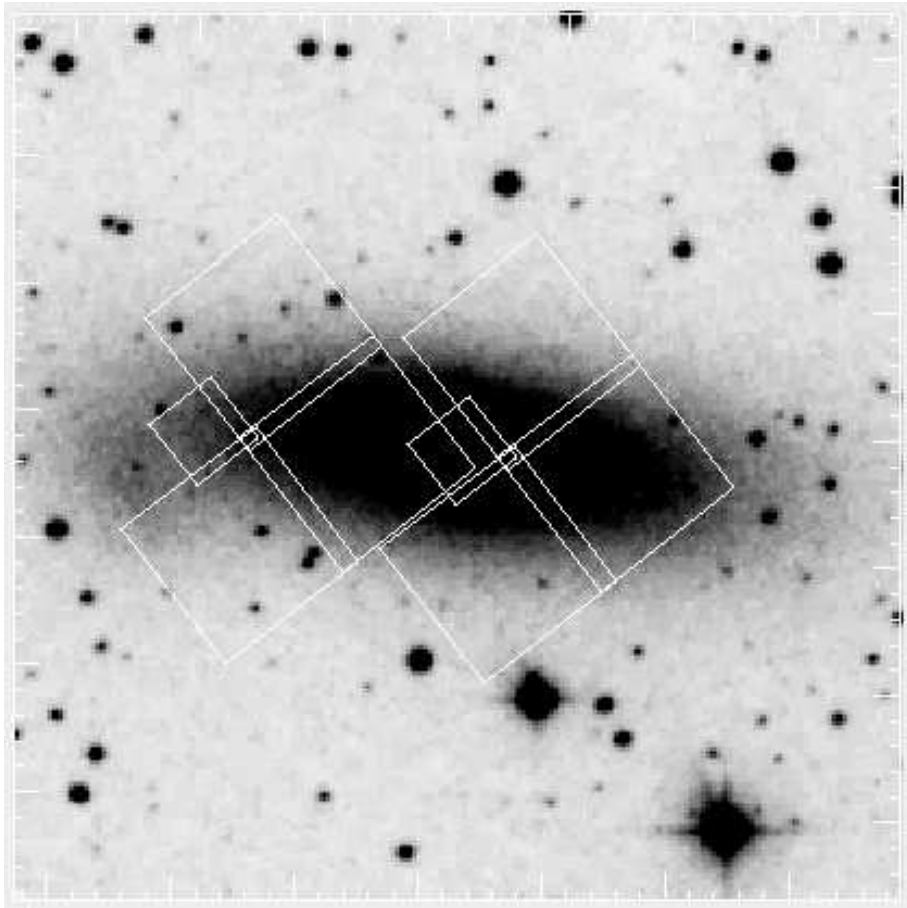


Fig. 1.— Our two WFPC2 pointings on NGC 1023, with north up and east to the left. The dwarf companion NGC 1023A is seen as an extension to the E.

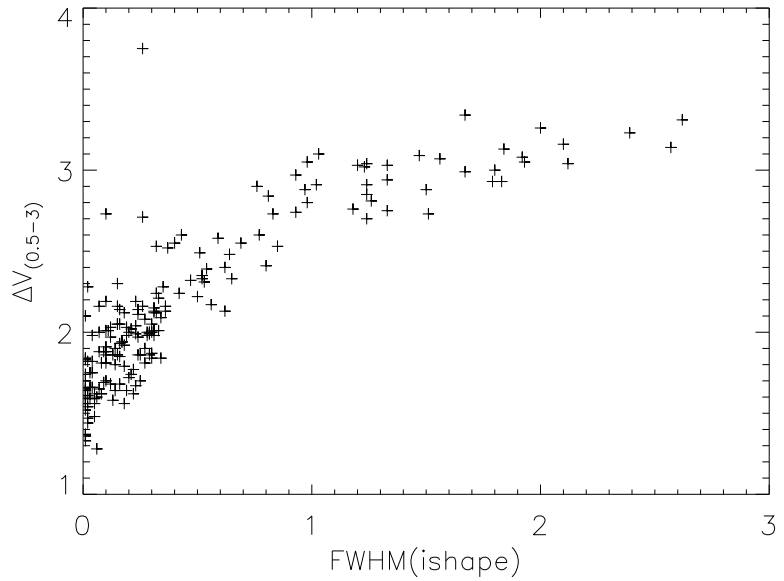


Fig. 2.— The  $\Delta_{0.5-3}$  index, defined as the difference between magnitudes measured through  $r = 3$  and  $r = 0.5$  pixel apertures on an  $F555W$  image, plotted against FWHM estimates by `ishape` for objects brighter than  $V = 24$ .

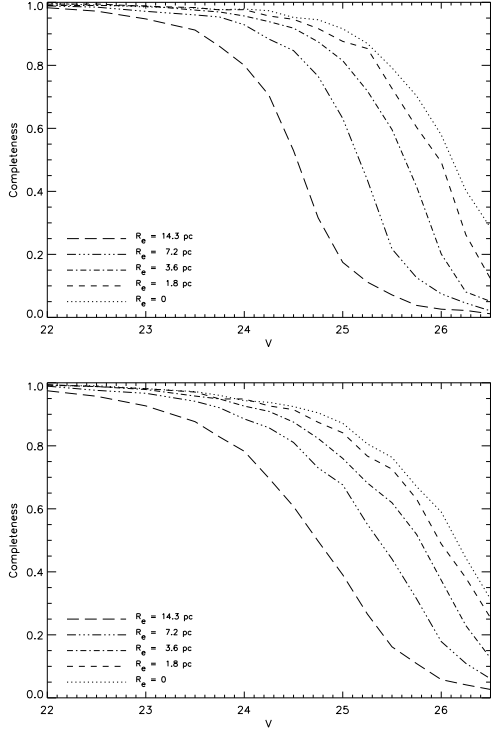


Fig. 3.— Completeness functions for the WF chips in the center (left) and east (right) pointings, shown for cluster FWHM values of 0, 0.25, 0.50, 1.0 and 2.0 pixels (corresponding to  $R_e = 0, 1.8, 3.6, 7.2$  and 14.2 pc, respectively). As this figure demonstrates, the completeness corrections depend strongly on cluster size.

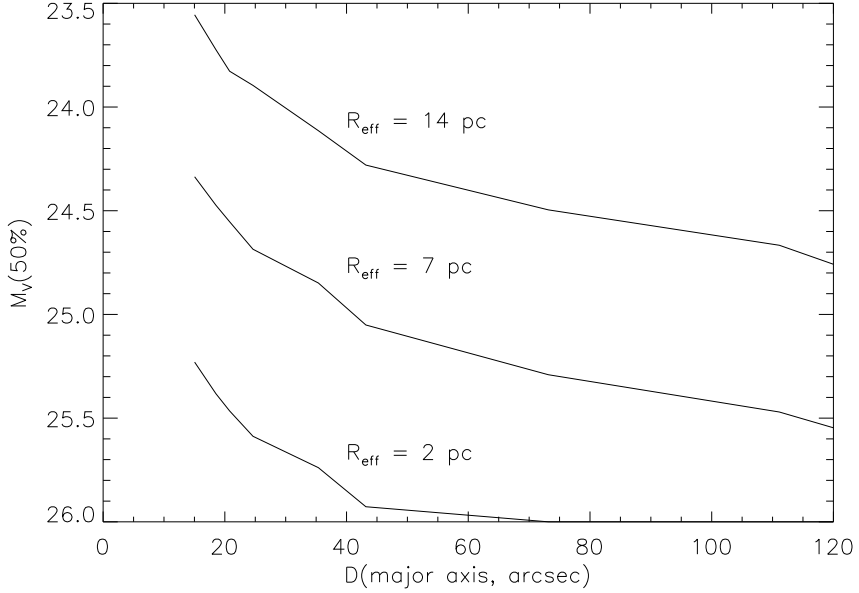


Fig. 4.— 50% completeness limits as a function of distance from the center of NGC 1023 along the major axis. Curves are shown for three different object sizes:  $R_e = 2$  pc, 7 pc and 14 pc.

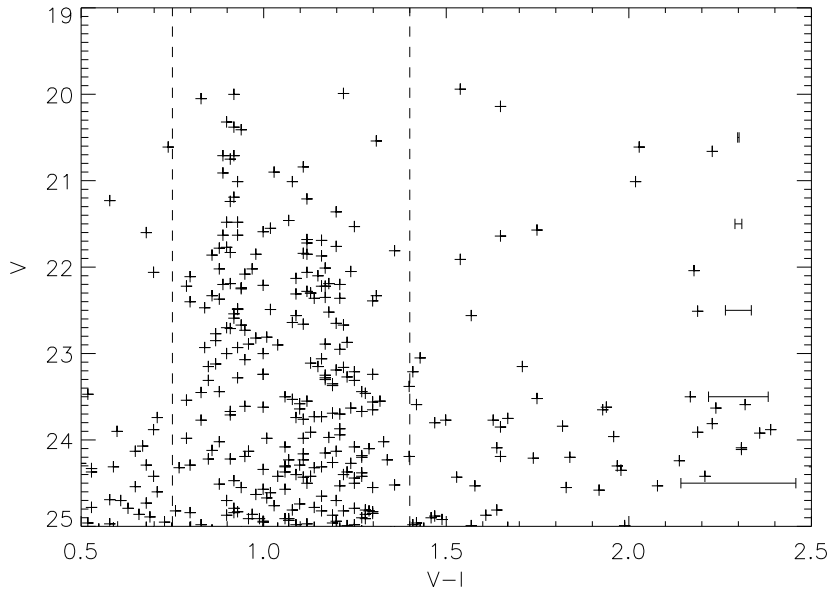


Fig. 5.— A  $V-I, V$  color-magnitude diagram for all objects detected in the two HST pointings on NGC 1023. Two peaks in the color distribution, at  $V-I = 0.92$  and at  $V-I = 1.19$  are readily distinguished. Photometric errors are indicated by the error bars at  $V-I = 2.3$ .

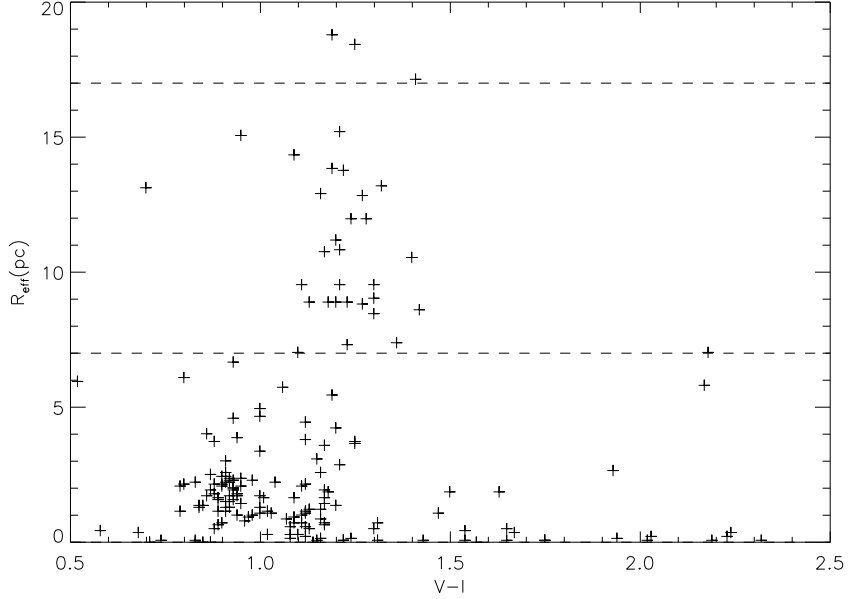


Fig. 6.— Effective radii (in pc) as a function of  $V - I$  color for objects brighter than  $V = 24$ . Cluster sizes were measured using the `ishape` algorithm (Larsen, 1999) assuming King  $c = 30$  profiles. Dashed lines mark the cuts applied in the selection of regular globular cluster candidates and “fuzzy” disk clusters.

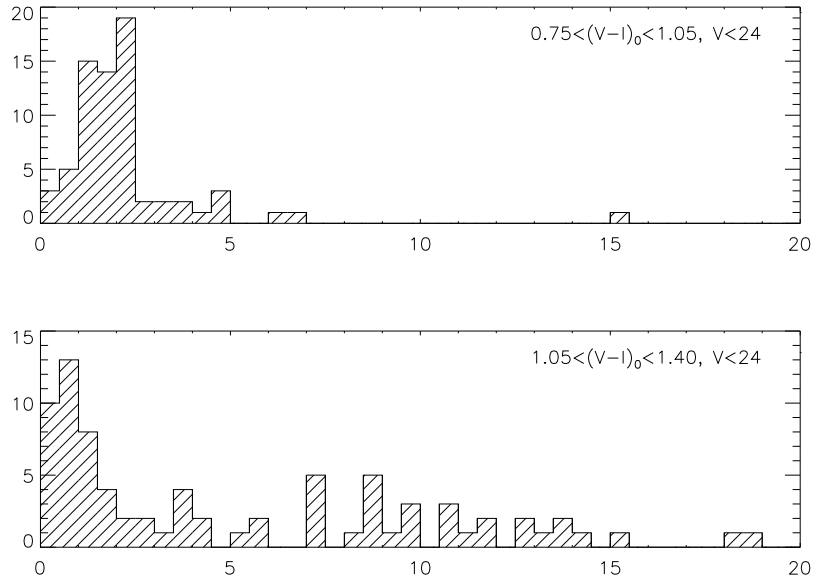


Fig. 7.— The size distribution for blue (top) and red (bottom) objects with  $V < 24$ . The majority of red objects are somewhat smaller than the blue ones, but the size distribution of red objects has a tail extending up to  $R_e \sim 15$  pc.

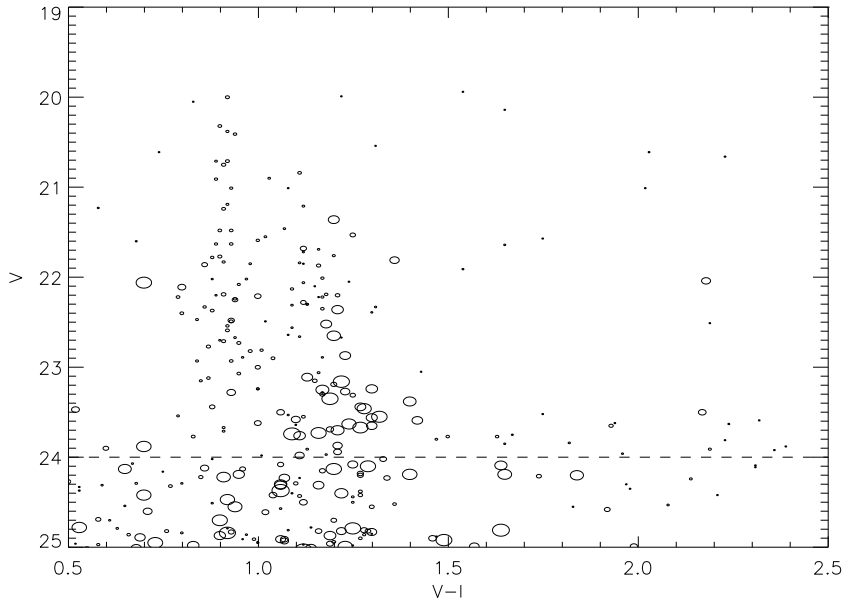


Fig. 8.— Color-magnitude diagram with symbol sizes representing the object sizes measured by `ishape`. Note the concentration of faint extended objects near  $V = 23.5$  and  $V-I = 1.2$ . The horizontal line indicates the magnitude limit above which cluster sizes are accurate to better than  $\pm 30\%$ .

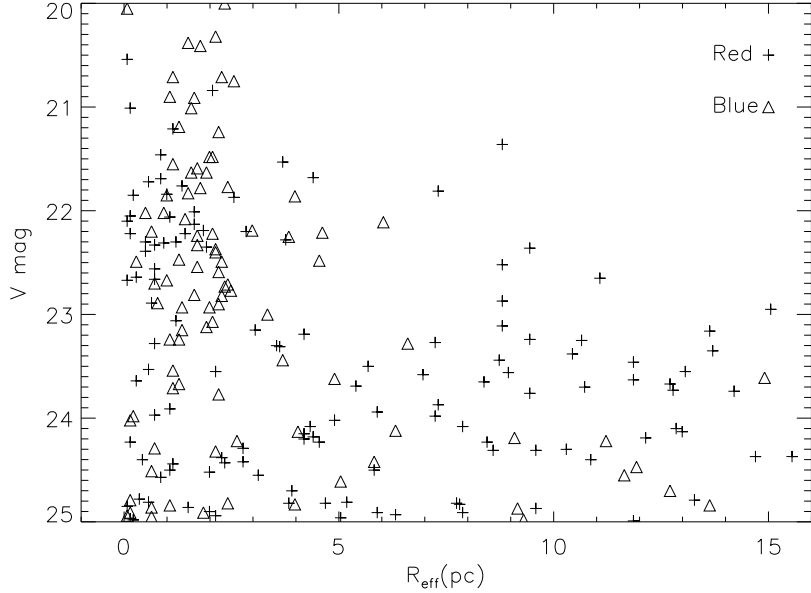


Fig. 9.—  $V$  magnitudes versus cluster sizes. Red clusters ( $V - I > 1.05$ ) are shown with plus markers and blue clusters with triangles. Qualitatively, this plot shows a striking resemblance to Fig. 1 of van den Bergh (1996) although extended clusters appear to be much more numerous in NGC 1023.

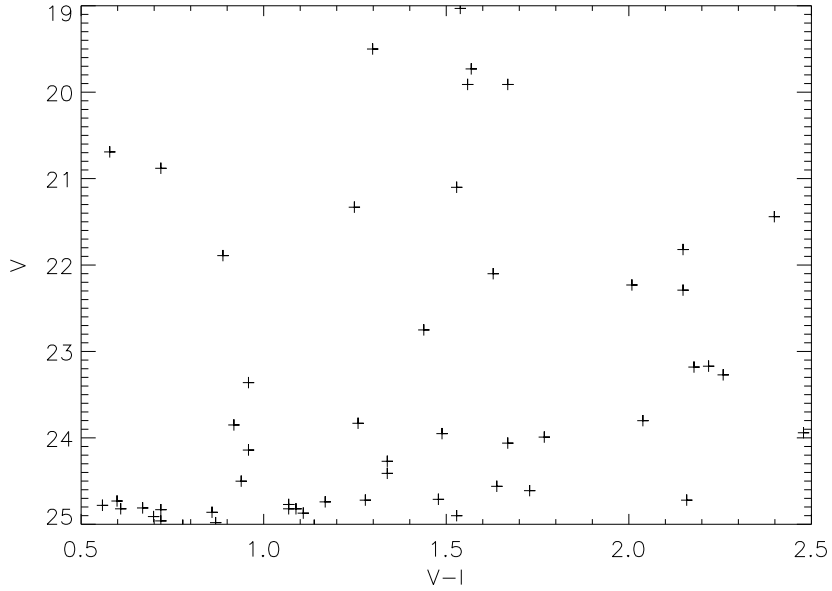


Fig. 10.— Color-magnitude diagram for the comparison field located about 2 degrees from NGC 1023.

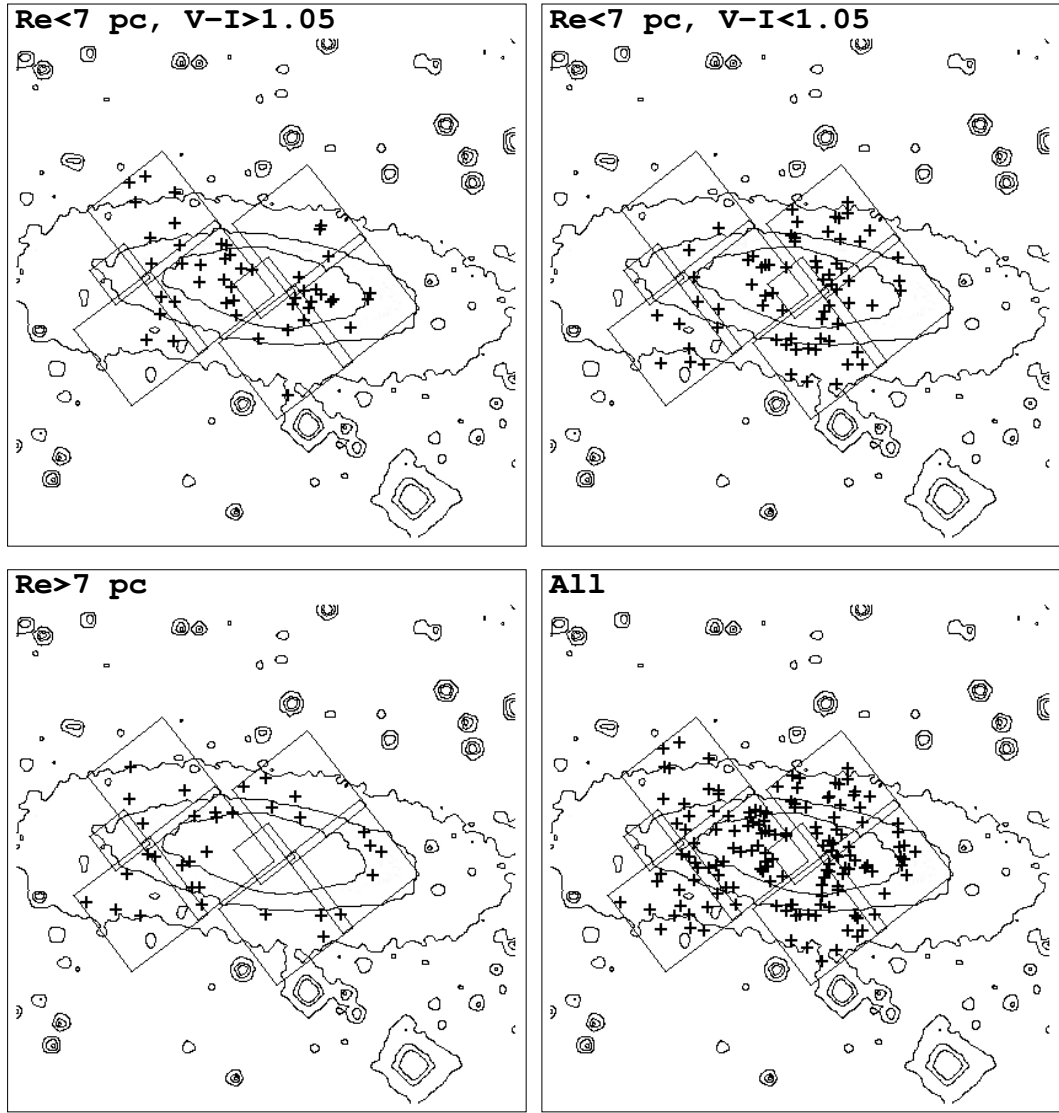


Fig. 11.— *The spatial distribution of different object types.*

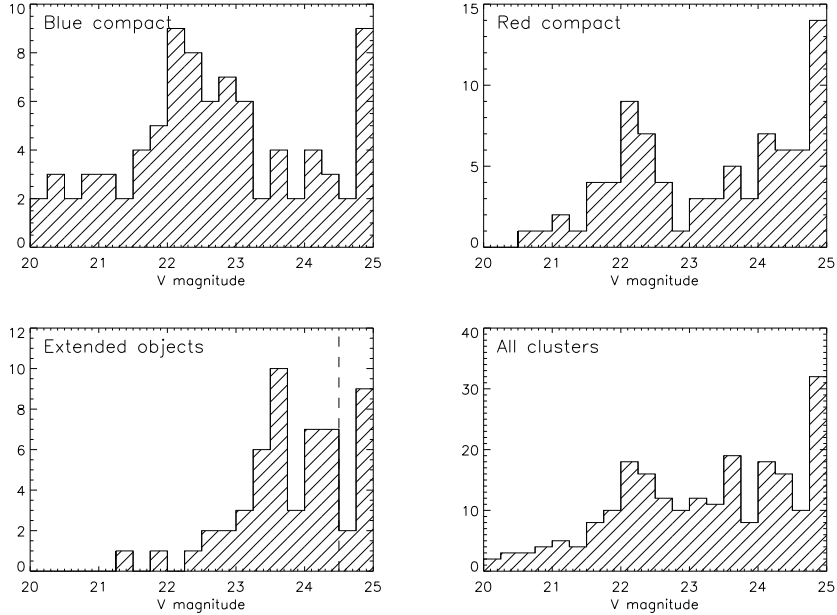


Fig. 12.— *Luminosity functions for the 3 cluster populations in NGC 1023. Approximate 50% completeness limits are indicated by the dashed lines. The brighter 50% limit for the extended clusters is due to their larger sizes. For the compact objects (upper panels) the 50% completeness limits are outside the plotted range.*

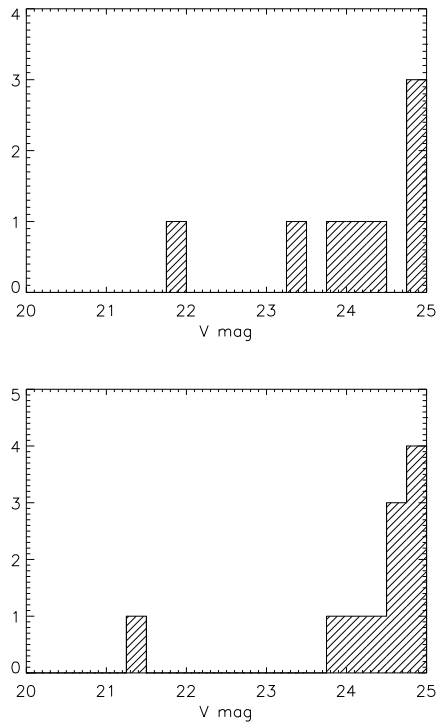


Fig. 13.— Luminosity functions for blue (left) and red (right) objects in the comparison field.

Table 1: Aperture corrections for different model profiles convolved with the `TinyTim` PSF and diffusion kernel. The FWHM are in pixel units. Equivalent  $R_e$  values are given for a distance of 9.9 Mpc. The notation  $5 \rightarrow 3$  refers to the aperture correction from an  $r = 5$  pixels to an  $r = 3$  pixels aperture.

Profile	$R_e$ (pc)	F555W			F555W–F814W		
		$5 \rightarrow 3$	$5 \rightarrow 2$	$30 \rightarrow 5$	$5 \rightarrow 3$	$5 \rightarrow 2$	$30 \rightarrow 5$
<b>King <math>c = 30</math></b>							
FWHM = 0.00	0.0	−0.060	−0.178	−0.09	0.015	0.031	0.01
	0.10	0.7	−0.061	−0.185	−0.09	0.016	0.031
	0.25	1.8	−0.079	−0.248	−0.09	0.015	0.030
	0.50	3.5	−0.157	−0.406	−0.11	0.014	0.027
	1.00	7.1	−0.276	−0.625	−0.24	0.013	0.024
	2.00	14.2	−0.426	−0.899	−0.52	0.011	0.020
<b>MOFFAT15</b>							
FWHM = 0.00	0.0	−0.060	−0.178	−0.09	0.015	0.031	0.01
	0.10	0.5	−0.071	−0.205	−0.10	0.016	0.030
	0.25	1.4	−0.093	−0.253	−0.12	0.015	0.029
	0.50	2.7	−0.127	−0.329	−0.16	0.014	0.028
	1.00	5.4	−0.196	−0.481	−0.23	0.015	0.027
	2.00	10.8	−0.335	−0.758	−0.38	0.011	0.022

Table 2: Results of maximum-likelihood fits of Gaussian and  $t_5$  functions to the luminosity functions of red and blue globular clusters. The errors in  $M_{\text{TO}}(V)$  do not include the  $\pm 0.14$  mag uncertainty on the distance modulus.  $P$  is the Kolmogorov-Smirnov probability that the data are drawn from a parent distribution with the specified parameters.

	Gaussian			$t_5$		
	$M_{\text{TO}}(V)$	$\sigma_V$	$P$	$M_{\text{TO}}(V)$	$\sigma_V$	$P$
Blue ( $0.75 < V-I < 1.05$ )	$-7.58_{-7.36}^{7.72}$	$1.12_{-1.03}^{1.33}$	0.991	$-7.56_{-7.37}^{7.70}$	$0.99_{-0.90}^{1.20}$	0.999
Red ( $1.05 < V-I < 1.40$ )	$-7.37_{-7.09}^{7.50}$	$0.97_{-0.89}^{1.25}$	0.352	$-7.42_{-7.19}^{7.56}$	$0.86_{-0.78}^{1.12}$	0.529
Red + Blue	$-7.48_{-7.32}^{7.59}$	$1.07_{-1.00}^{1.24}$	0.906	$-7.49_{-7.37}^{7.60}$	$0.94_{-0.86}^{1.08}$	0.943
Red + Blue + Extd	$-6.98_{-6.85}^{7.13}$	$1.27_{-1.18}^{1.36}$	0.695	$-7.07_{-6.95}^{7.21}$	$1.09_{-1.00}^{1.19}$	0.637